ChemistrySelect

Research Article
doi.org/10.1002/slct.202502428

Chemistry
Europe
European Chemical
Societies Publishing

www.chemistryselect.org

Electronic, Optical, and Thermoelectric Qualities of Sr$_2$p$_7$br Double Zintl Salt with Heptaphosphanortricyclane Configuration: A Promising Candidate for Thermoelectric and Photonic Devices

Missoum Radjai,*[a] Saber Saad Essaoud,[b, c] Abdelmadjid Bouhemadou,*[d] Djamel Allali,[e, f] Abdelhak Bedjaoui,[g] Mohammed Elamin Ketfi,[h] and Saad. Bin-Omran[i]

In this investigation, the structural, electronic, optical, and thermoelectric qualities of Sr$_2$P$_7$Br, a double Zintl salt with a heptaphosphanortricyclane configuration, were assessed using the first-principles FP-LAPW approach. The exchange-correlation interactions were simulated using the GGA-PBEsol method to analyze the structural properties, whereas the TB-mBJ functional was utilized to assess the electronic, optical, and thermoelectric features. The Birch–Murnaghan equation of state was used to fit the total energy versus unit cell volume in order to determine the relaxed lattice parameter, bulk modulus, and its pressure derivative. The calculated equilibrium structural parameters and bulk modulus agree with the corresponding experimental and theoretical values. Based on the results of the computed density of states and band structure, Sr$_2$P$_7$Br is classed as a wide bandgap semiconductor with an indirect bandgap (R-M) of 4.14 eV. The QTAIM descriptors computed at critical points forecast the covalent and ionic characteristics of the bonds between the compound's atoms. The optical coefficients, comprising the complex dielectric function, reflectivity, complex refractive index, absorption coefficient, and electron energy loss, were examined across an energy spectrum of 0–40 eV. The thermoelectric coefficients were determined utilizing the semi-classical Boltzmann transport model, assuming that the relaxation time remains constant. The results show that the figure of merit is about 0.9 at 600 K.

1. Introduction

Zintl materials are a notable category of intermetallic materials connecting ionic and covalent materials. The materials exhibit complex structures and notable electronic properties. These compounds generally arise when electropositive metals, including alkali and alkaline earth metals, interact with more electronegative p-block elements, especially those belonging to the groups 13–16 of the periodic table. The distinctive properties of Zintl phases render them significant for theoretical research and practical applications.[1–17] Due to their crystal structures and electrical configurations, certain Zintl phases possess unique optoelectronic and thermoelectric capabilities.[18] These materials exhibit low lattice thermal conductivities because of their intricate anionic frameworks that scatter phonons, as well as high electrical conductivity, which are vital for thermoelectric performance.[19,20] Zintl phases demonstrate promising thermoelectric properties, making them ideal for waste-heat recovery or solid-state cooling applications.[19,20] Some Zintl phases feature variable band gaps and significant light absorption, rendering them useful in optoelectronics, such as infrared detectors, photovoltaics, and LEDs.[21] Zintl phases provide sustainable

[a] M. Radjai
Laboratory of Physics of Experimental Techniques and Their Applications (LPTEAM), University of Medea, Medea 26000, Algeria
E-mail: radjai.missoum@univ-medea.dz

[b] S. S. Essaoud
Department of Physics, Faculty of Sciences, University of M'sila, M'Sila 28000, Algeria

[c] S. S. Essaoud
Laboratory of materials and renewable energy, Faculty of science, University of M'sila, M'Sila 28000, Algeria

[d] A. Bouhemadou
Laboratory for Developing New Materials and their Characterizations, Department of Physics, Faculty of Science, Ferhat Abbas University – Setif 1, Setif 19000, Algeria
E-mail: abdelmadjid_bouhemadou@univ-setif.dz

[e] D. Allali
Laboratory of Materials and Renewable Energies, University of M'sila, M'Sila 28000, Algeria

[f] D. Allali
University Pole, Faculty of Technology, University of M'sila, M'Sila 28000, Algeria

[g] A. Bedjaoui
Department of Technology, Faculty of Technology, University of Bejaia, Bejaia 6000, Algeria

[h] M. E. Ketfi
Department of Electronics, Faculty of Technology, University of M'sila, M'Sila 28000, Algeria

[i] S. Bin-Omran
Department of Physics and Astronomy, College of Science, King Saud University, P.O. Box 2455, Riyadh 11451, Saudi Arabia

ChemistrySelect

Research Article
doi.org/10.1002/slct.202502428

Chemistry Europe
European Chemical
Societies Publishing

alternatives to lead chalcogenides owing to their non-toxicity, abundance in nature, and structural versatility. Researchers aim to employ these materials to develop hybrid devices that capture light and heat energy, thereby enhancing energy harvesting, wearable electronics, and high-efficiency thermoelectric–optoelectronic systems.[22,23]

Double Zintl salt compounds featuring the heptaphosphanortricyclane structure are a notable category of Zintl phases that have garnered significant interest from researchers. Dolyniuk and Kovnir[24] showed that the Zintl salts Ba_2P_7Br and Ba_2P_7I had isostructural properties with the heptaphosphanortricyclane structure. In a following work, Dolyniuk et al.[25] effectively synthesized three novel strontium phosphide-halides, namely Sr_2P_7Cl, Sr_2P_7Br, and Sr_2P_7I, and elucidated their crystalline structures by Rietveld analysis of powder X-ray diffraction spectra. They also analyzed their electronic qualities, including the energy band dispersions and density of states diagrams, using first-principles calculations. Their research indicates that the Sr_2P_7X materials (X = Cl, Br, and I) crystallize in a cubic chiral configuration, specifically within space group $P2_1/3$ (n. 198).

Aside from the findings presented by Dolyniuk et al.[25] about the structural features and band structure of strontium phosphide-halide Sr_2P_7Br, information on its physical qualities is limited. Sr_2P_7Br has advantageous physical properties pertinent to various applications. Therefore, it is essential to perform a thorough research of the unexplored physical characteristics of the Sr_2P_7Br double Zintl salt with a heptaphosphanortricyclane structure for potential future uses. This compels us to conduct comprehensive analyses of the electronic structure, optical spectra, and thermoelectric qualities for the Sr_2P_7Br double Zintl salt through first-principles simulations. To do this, we employed the cutting-edge full-potential linearized augmented plane wave (FP-LAPW) approach, an advanced approach grounded in density functional theory (DFT). The thermoelectric coefficients of the chemicals examined were evaluated using Boltzmann's semi-classical transport model, assuming a constant relaxation time.

2. Calculation Settings

Quantum mechanical computations were conducted using the full-potential linearized augmented plane wave (FP-LAPW) approach, incorporated into the WIEN2k software.[26] The well-known functional GGA-PBEsol[27] was employed to describe the exchange-correlation (XC) energy for structural property calculations, whereas the TB-mBJ potential[28,29] was applied for the same aim in electronic structure and related property calculations. A spherical harmonic function up to $l_{max} = 10$ was employed to construct the wave functions inside the muffin-tin spheres, alongside a plane wave function restricted by a maximum reciprocal lattice vector $K_{max} = 10/R_{MT}^{min}$, where R_{MT}^{min} is the minimum muffin-tin sphere radius. In periodic systems, the electronic wave functions are Bloch functions, defined in reciprocal space (k-space). Calculating physical characteristics involves integrations over the Brillouin zone, which consists of continuous

k-points, to involve the contributions of all electrons. Since it is practically impossible to perform calculations by considering the contribution of every electronic state, and in order to conserve computation time, these integrations are approximated by assuming a finite number of k-points. Generally, the k-point mesh is analyzed using the Monkhorst–Pack scheme to assure uniform sampling of the Brillouin zone. Naturally, the greater the number of selected states, the higher the accuracy of the calculations, but the longer the computation time. To limit the computation time, we should reduce the number of k-points as much as possible without sacrificing the accuracy of the calculation outcomes. To determine the correct number of k-points for calculating the structural properties and associated properties, we look at how the total energy varies with different amounts of k-points and then choose the number of k-points assuring the convergence of total energy. In this study, we used a 10 × 10 × 10 Monkhorst–Pack grid to ensure good convergence of total energy. To calculate other properties, such as curves of density of states, optical spectra, and thermoelectric characteristics, we should employ dense k-points to ensure accurate results for these properties. The chosen number of k-points for computing these attributes is determined by the convergence of their curves in relation to the number of k-point mesh. In this study, a 50 × 50 × 50 Monkhorst–Pack grid to ensure accurate calculations of the state density curves, optical spectra, and thermoelectric coefficients. The total energy calculations were accomplished with a convergence criterion of 10^{-5} Ry. Sr_2P_7Br's atomic sites were allowed to relax freely until no atom sensed a force greater than 5×10^{-4} Ry/Bohr.

The complex dielectric function ($\varepsilon(\omega)$) which shows how matter reacts to electromagnetic waves,[30] was determined using the optical properties calculation package provided by the WIEN2k computer program. The real component of $\varepsilon(\omega)$, namely $\varepsilon_1(\omega)$, characterizes the electromagnetic radiation dispersion inside the matter, and the imaginary component, $\varepsilon_2(\omega)$, characterizes the medium's absorption of radiation.[31] Theoretically, $\varepsilon_2(\omega)$ is calculated by summing the components of the electric dipole operator matrix associated with electronic transitions from filled to empty electronic levels.[25]

$$\varepsilon_2(\omega) = \frac{Ve^2}{2\pi\hbar m^2\omega^2} \int d^3k \sum_{nn'} \left|\langle kn| e \cdot \nabla |kn'\rangle\right|^2 f(kn)$$
$$\times \left[1 - f(kn')\right] \delta\left(E_{kn} - E_{kn'} - \hbar\omega\right)$$

In this context, $\hbar\omega$ represents the energy of the incident photon, $|kn\rangle$ corresponds to the eigenfunction with the eigenvalue E_{kn}, $f(kn)$ is the Fermi distribution function, the integral symbol represents integration over the first Brillouin zone (BZ), and $\langle kn|e \cdot \nabla|kn'\rangle$ represents the momentum dipole components. The $\varepsilon_1(\omega)$ spectrum is derived from $\varepsilon_2(\omega)$ through the Kramers–Kronig relationship.[30] $\varepsilon_1(\omega) = 1 + \frac{2}{\pi}P\int_0^\infty \frac{\omega'\varepsilon_2(\omega')}{\omega'^2-\omega^2}d\omega'$ where, P implies the principal value of the integral. The linear optical parameters, including the absorption coefficient ($\alpha(\omega)$), reflectivity ($R(\omega)$) and refractive index ($n(\omega)$), extinction coefficient ($k(\omega)$) and energy-loss function ($l(\omega)$) are determined from the $\varepsilon_1(\omega)$ and $\varepsilon_2(\omega)$

ChemistrySelect

Research Article
doi.org/10.1002/slct.202502428

Chemistry Europe
European Chemical
Societies Publishing

components of $\varepsilon(\omega)$.[32]

$$\alpha(\omega) = \sqrt{2}\omega\left[\sqrt{\varepsilon_1^2(\omega) + \varepsilon_2^2(\omega)} - \varepsilon_1(\omega)\right]^{1/2}$$

$$n(\omega) = \frac{1}{\sqrt{2}}\left[\sqrt{\varepsilon_1^2(\omega) + \varepsilon_2^2(\omega)} + \varepsilon_1(\omega)\right]^{1/2}$$

$$k(\omega) = \left[-\frac{\varepsilon_1(\omega)}{2} + \frac{\sqrt{\varepsilon_1^2(\omega) + \varepsilon_2^2(\omega)}}{2}\right]^{1/2}$$

$$R(\omega) = \left|\frac{\sqrt{\varepsilon(\omega)} - 1}{\sqrt{\varepsilon(\omega)} + 1}\right|^2$$

$$L(\omega) = \left|\frac{\varepsilon_2(\omega)}{\varepsilon_1^2(\omega) + \varepsilon_2^2(\omega)}\right|$$

The thermoelectric characteristics of the examined compound were assessed utilising the BoltzTraP2 software,[33] an application of the semi-classical Boltzmann transport model under the assumptions of a rigid band model and a constant relaxation time.[34,35] The Seebeck coefficient (*S*; called also thermopower), which quantifies the ratio between the electrical potential and the temperature gradient ($S = \Delta V/\Delta T$), and the electrical conductivity (σ) as functions of absolute temperature (*T*) and chemical potential (μ) can be calculated by integrating the transport distribution.[27]

$$\sigma_{\alpha\beta}(T, \mu) = \frac{1}{\Omega}\int\sigma_{\alpha\beta}(E)\left[\frac{\partial f_\mu(T, E)}{\partial E}\right]dE$$

$$S_{\alpha\beta}(T, \mu) = \frac{1}{eT\Omega\sigma_{\alpha\beta}(T, \mu)}\int\sigma_{\alpha\beta}(E)(E - \mu)\left[\frac{\partial f_\mu(T, E)}{\partial \epsilon}\right]dE$$

Here, Ω is the volume of the unit cell, *f* is the Fermi–Dirac distribution function and *e* is the electron charge. The energy projected transport distribution $\sigma_{\alpha\beta}(\varepsilon)$, which contains the system dependent information, can be expressed as.

$$\sigma_{\alpha\beta}(E) = \frac{e^2}{N}\sum_{i,k}\tau_{i,k}v_\alpha(i, k)v_\beta(i, k)\frac{\delta(E - E_{i,k})}{\delta E}$$

here *N* is the number of k-points, *i* is the band index, *k* is the wave vector, and $v_\alpha(i, \mathbf{k})$ is the group velocity, which can be obtained from the band structure calculation as.

$$v_\alpha(i, k) = \frac{1}{\hbar}\frac{\delta E_{i,k}}{\delta k_\alpha}$$

The wave vector dependent relaxation time ($\tau_{i,k}$) appearing in the expression of $\sigma_{\alpha\beta}(\varepsilon)$ is difficult to be determined from first-principles calculations and hence the equation of $\sigma_{\alpha\beta}(\varepsilon)$ is solved under constant relaxation time approximation (RTA).[27] Within the RTA, the Seebeck coefficient can be calculated without any adjustable parameters; however, the electrical
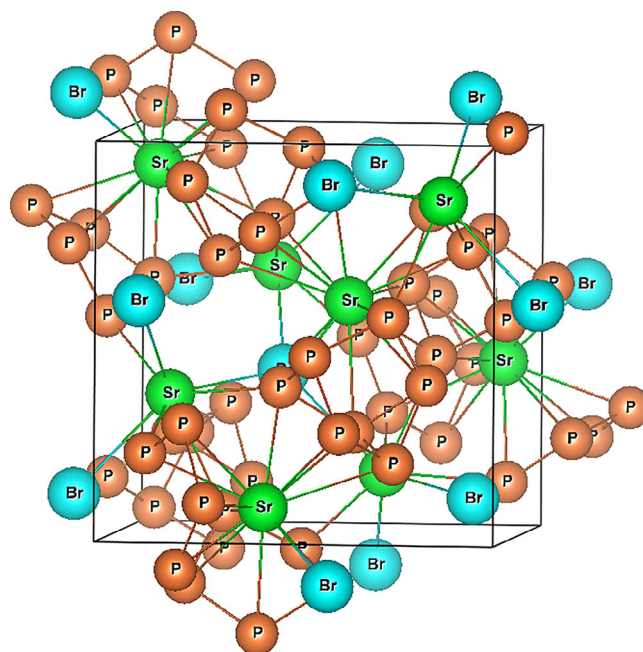

Figure 1. The strontium phosphide halide, Sr_2P_7Br, unit-cell crystal structure.

conductivity has to be calculated with respect to the relaxation time.

3. Presentation and Discussion of the Obtained Results

3.1. Structural Qualities

The compound strontium phosphide-halide Sr_2P_7Br crystallizes in a chiral cubic structure within the space group $P2_1/3$(n. 198) with $Z = 4$. In the unit cell, there exist two inequivalent atomic places for strontium (Sr1 and Sr2), three inequivalent atomic sites for phosphorus (P1, P2, and P3), and one atomic site for the halogen bromine (Br). Figure 1 illustrates a unit cell of the Sr_2P_7Br crystal. The electron-balanced formula of the Zintl salt Sr_2P_7Br is $(Sr^{2+})_2(P_7^{-3})(Br^{1-})$.

As depicted in Figure 2, the computed total energy (*E*) versus unit cell volume (*V*) utilizing the GGA-PBEsol XC-functional were analyzed using the Murnaghan's equation of state.[36]

$$E(V) = E_0 + \frac{9B_0V_0}{16}$$

$$\times\left\{\left[\left(\frac{V_0}{V}\right)^{\frac{2}{3}} - 1\right]^3 B' + \left[\left(\frac{V_0}{V}\right)^{\frac{2}{3}} - 1\right]^2\left[6 - 4\left(\frac{V_0}{V}\right)^{\frac{2}{3}}\right]\right\}$$

here, V_0 is the equilibrium unit cell volume, E_0 is the total energy of the equilibrium unit cell, *B* is the bulk module and *B'* is the first pressure derivative of *B*. The fitting process produced the volume of the equilibrium unit cell (V_0), bulk modulus (*B*), and first pressure derivative of *B* (*B'*), which are listed in Table 1.

The predicted values for the optimized lattice parameter (*a*), bulk modulus (*B*), and the first pressure derivative of *B* (*B'*)
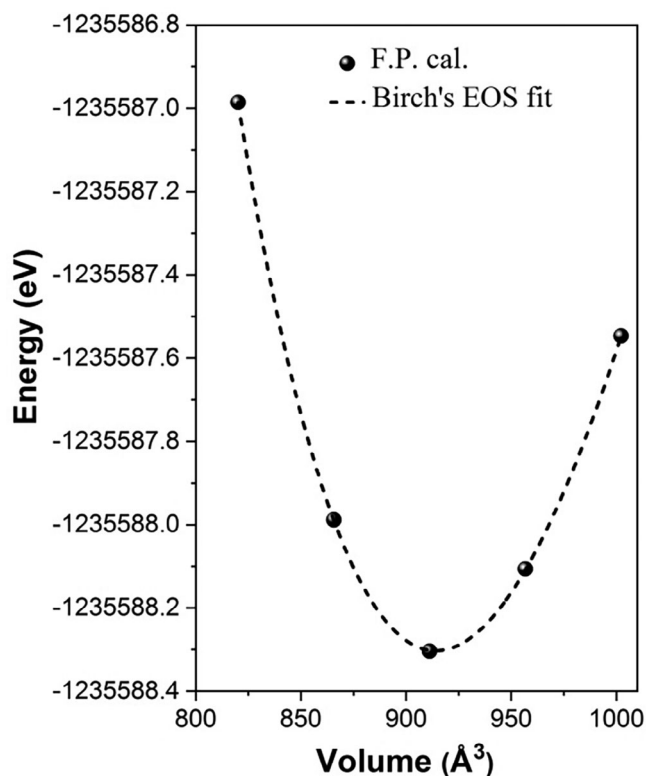
ChemistrySelect

Research Article
doi.org/10.1002/slct.202502428

Chemistry Europe
European Chemical
Societies Publishing

Figure 2. The Sr_2P_7Br compound's total energy (E) in relation to its unit cell volume (V). The dashed line shows the results of fitting the E–V data to the Birch equation of state (Birch's EOS fit), while the symbols show the results of first-principles calculations (F.P. cal.).

Table 1. The Sr_2P_7Br compound's optimized lattice parameter (a, in Å), bulk modulus (B, in GPa), and its first pressure derivative (B'). The available data in the literature for a, B, and B' are provided for comparison.

Property	Present	Other[24]	Other[37]
a	9.7053	9.7889,	9.6947
B	34.7	–	33.79
B'	5.32	–	5.25

align with the results of previous theoretical studies,[18,34] thereby reinforcing the validity of the current work.

3.2. Electronic Characteristics

3.2.1. Energy Band Dispersions

A material's electronic structure contains crucial data about the properties that are important from the perspective of applications.[38] We analyzed the electronic structure and related characteristics of cubic Sr_2P_7Br by calculating its electronic energy band dispersions along the high-symmetry lines in BZ, as illustrated in Figure 3. The compound Sr_2P_7Br is identified as a semiconductor with an indirect bandgap, where the valence band maximum (VBM) is found in the middle of the R → M line in the Brillouin zone (BZ), and the conduction band mini-
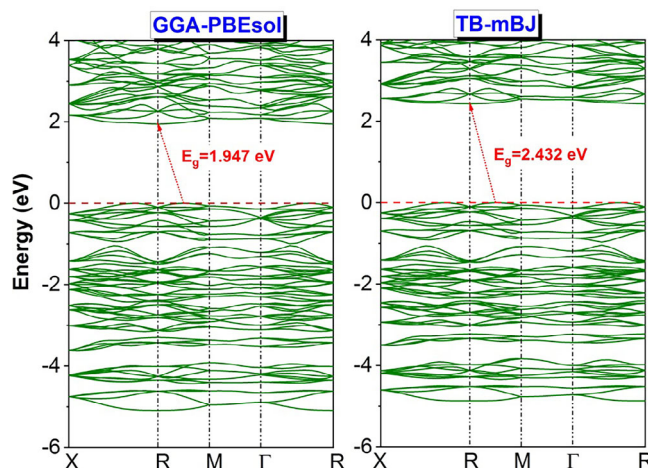

Figure 3. Electronic band structure computed utilizing GGA-PBEsol and TB-mBJ approaches for the chemical Sr_2P_7Br. The arrow denotes the fundamental band gap.

mum (CBM) is situated at the R point in the BZ. The value of the fundamental energy bandgap determined utilizing the TB-mBJ functional ($E_g^{TB-mBJ} = 2.432 eV$) exceeds that obtained utilizing the GGA-PBEsol ($E_g^{GGA-PBEsol} = 1.947 eV$) by approximately 25%. The DFT-GGA computations are known to underestimate the energy bandgap value, prompting the development of the TB-mBJ potential to address this deficiency. The TB-mBJ raises the conduction band and alleviates the underestimation of the energy bandgap. It is important to note that a previously published band gap, $E_g^{TB-LMTO} = 2.1$ eV,[19] derived using the TB-LMTO-ASA technique, falls within the range of our projected band gap values, E_g^{TB-mBJ} and $E_g^{GGA-PBEsol}$.

3.2.2. Charge-Carrier Effective Masses

Effective masses of holes and electrons are crucial components in both experimental and theoretical evaluations of some characteristics of materials. Charge-carrier effective masses significantly influence the material's transport properties. Numerical estimations of the effective masses of charge carriers were derived in this study by fitting the energy-band dispersion at the band edges to a parabolic model. In this study, numerical estimates of charge-carrier effective masses were obtained via the fit of the energy-band dispersion $E(k)$ at the band extremes to a parabolic model. The effective mass, denoted as m^* and expressed in terms of m_0, mass of an electron at rest, is subsequently determined using the following formula.

$$\frac{1}{m^*} = \frac{m_0}{\hbar^2} \frac{\partial^2 E(k)}{\partial k^2}$$

A dense k-point sample was utilized to compute the energy band dispersion. Only the k-points closest to the extremes were employed for the calculation of effective masses. As illustrated in Figure 3, the electronic states near the VBM point demonstrate greater dispersion than those near the CBM point. This suggests that the effective masses of electrons exceed those of holes. The numerical estimations of effective masses of holes at the
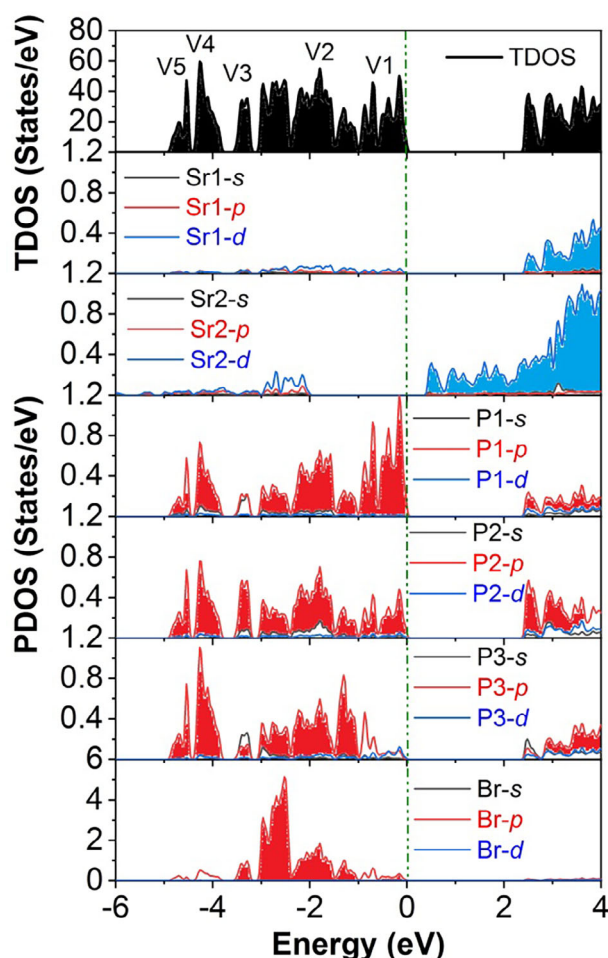
ChemistrySelect

Research Article
doi.org/10.1002/slct.202502428

Chemistry Europe
European Chemical
Societies Publishing

Figure 4. The computed total density of states (TDOS) and partial density of states (PDOS) diagrams for the chemical Sr_2P_7Br.

VBM point, located between the *R* and *M*-points in BZ, toward the *R* and *M*-points, utilizing the TB-mBJ (GGA-PBEsol) approach to model the XC-potential, are: $m_h^*((R-M) \rightarrow R) = 0.5253(0.3541)$ and $m_h^*((R-M) \rightarrow M) = 0.2776$ (0.3541). The calculated values of electron effective masses at the CBM point, positioned at the R-point in BZ, toward the X and M points, using the TB-mBJ (GGA-PBEsol) approach are $m_e^*(R \rightarrow M) = 1.1024(1.1830)$ and $m_e^*(R \rightarrow X) = 1.7343(0.998)$. It is noted that electrons are heavier than holes, suggesting that the mobility of electrons is markedly inferior to that of holes. The anisotropy of the charge carrier masses is evident from the values calculated at the VBM and CBM in various orientations within the BZ.

3.2.3. Density of States Diagrams

We computed the diagrams showing the total density of states (TDOS) and *l*-decomposed atom-projected density of states (PDOS) within the energy range of −10–10 eV in order to elucidate the origins of electronic states in the Sr_2P_7Br compound's energy bands, as shown in Figure 4.

There are five possible sub-band divisions in the valence bands that extend from about −5–0 eV. The hybridizations of P-*p* orbitals with Br-p orbitals and P-*p* orbitals from non-equivalent

P locations result in the formation of the sub-bands V1, which span approximately from −1 eV to the Fermi level (0 eV). The V2 valence sub-bands, which extend from about −3–1 eV, comprise a hybridization of the Br-*p* states with the P-*p* states. Hybridization of the P-sp orbitals with the Br-sp orbitals generates the valence sub-bands V3, which range from −3.6–3.2 eV. Hybridization of P-*p* states gives rise to the valence band groups V4, ranging from −0.4–3.8 eV, and V5, spanning from −4.9–4.6 eV. The P-sp states generate a minor valence band group, situated between −7.8 and −7.0 eV, which is not illustrated for clarity. The hybridization observed among the P-*p* orbitals, and between the P-*p* and Br-*p* orbitals, indicates the existence of covalent bonding both among the P atoms and between the P and Br atoms. It is important to observe the subtle variation in the PDOS of the three inequivalent P atoms (P1, P2, and P3) resulting from their distinct environments within the crystal structure. The lowest part of the conduction band is mostly determined by the Sr-*d* states, with a small influence from the P-*p* states. This signifies the existence of ionic connections between the Sr cations and the P and Br anions. The various PDOS of P1, P2, and P3 atoms in Sr_2P_7Br demonstrate that it possesses both ionic and covalent bonds, which influence its electronic structure and thermoelectric performance. Covalent P—P interactions enhance the mobility of charge carriers, while ionic regions create specific energy levels and scatter sound waves, thereby increasing the Seebeck coefficient and reducing the lattice thermal conductivity. This combination positions Sr_2P_7Br as a possible candidate for high-performance thermoelectrics, particularly if modifications to its structure or the addition of other materials can improve the balance between delocalized and localized electronic states. The system demonstrates how we can harness different types of atoms in complex materials to advance improved energy conversion technologies.

3.2.4. Chemical Bonding Analysis

The characteristics of chemical bonding within a material can be clarified by analyzing the distribution of electron charge density. This study investigated the distribution of electron charge density within the crystal lattice of the compound in question, employing the Quantum theory of atoms in molecules (QTAIM)[39,40] as incorporated in the program CRITIC2.[41] The QTAIM methodology utilizes a range of descriptors at bond critical points (BCP), specifically ρ_b: electron charge density, $\nabla^2\rho_b$: Laplacian of ρ_b, H_b: local kinetic electron energy density, V_b: electronic potential energy density, and G_b: local total electron energy density, to determine the chemical bond nature. Furthermore, it integrates the bond lengths, d_{E1-E2}, the angle created by the termini E1 and E2 with the BCP, $\hat{\alpha} = E1 - BCP - E2$, the distance from the BCP to each atomic nucleus, r_i, and the attractor connectivity matrix to clarify the features of chemical bonding in the material. These descriptors play a vital role in determining the type of bond and revealing the stability of the compound. By examining the charge density, which reflects the charge distribution along the bond, we can confirm the covalent nature and strength of the bond if this density is high at the critical point of the bond. The negative sign of the Laplacian of the

ChemistrySelect

Research Article
doi.org/10.1002/slct.202502428

Chemistry Europe
European Chemical
Societies Publishing

Table 2. Topological and QTAIM descriptors at BCPs in Sr_2P_7Br. r_1, and r_2 are in Å. ρ_b is in e.Å^{-3}. $\nabla^2\rho_b$ is in e.Å^{-5}. V_b is in $a.u.$ G_b is in a.u. H_b is in a.u.

| Bond E1—E2	BCP coordinates			QTAIM descriptors									
	x	y	z	r_1	r_2	r_1/r_2	$\hat{\alpha}$	ρ_b	$\nabla^2\rho_b$	G_b	V_b	$|V_b|/G_b$	H_b
P—P	0.0266	0.1770	0.2610	2.0475	2.0460	1.0007	179.26	0.09092	0.02999	0.05778	−0.10806	1.87024	−0.05028
P—P	0.8723	0.4881	0.4221	2.0592	2.0580	1.0006	179.05	0.08908	0.03308	0.05653	−0.10479	1.85369	−0.04826
P—P	0.7922	0.6757	0.2350	2.1668	2.1666	1.0001	175.74	0.07752	0.05592	0.04979	−0.08560	1.71919	−0.03581
Sr—P	0.0216	0.0171	0.3203	2.8140	3.0322	0.9280	174.83	0.01982	0.05015	0.01253	−0.01252	0.99919	0.00001
Sr—Br	0.99860	0.0014	0.5014	3.0669	2.7822	1.1023	180.00	0.01952	0.05853	0.01382	−0.01300	0.94114	0.00081
Sr—P	0.9410	0.9410	0.9410	2.9840	2.8002	1.0656	180.00	0.01946	0.05004	0.01238	−0.01225	0.98963	0.00013
Sr—P	0.9331	0.2742	0.1521	3.0880	2.8485	1.0841	174.88	0.01864	0.04579	0.01139	−0.01134	0.99539	0.00005
Sr—P	0.2883	0.3645	0.7115	3.0574	2.8474	1.0738	179.04	0.01793	0.04407	0.01087	−0.01072	0.98650	0.00015
P—Br	0.3101	0.3349	0.2678	3.2226	3.2166	1.0018	165.51	0.01565	0.03555	0.00874	−0.00859	0.98280	0.00015
P—P	0.3775	0.0370	0.3856	3.4357	3.3817	1.0159	175.91	0.01133	0.02090	0.00512	−0.00502	0.98026	0.00010
Sr—Br	0.4670	0.7690	0.1239	3.0889	3.4524	0.8947	178.63	0.01126	0.02469	0.00574	−0.00531	0.92452	0.00043
P—Br	0.4374	0.4008	0.5899	3.5057	3.5039	1.0005	168.41	0.01119	0.02018	0.00497	−0.00490	0.98528	0.00007
P—P	0.8570	0.2875	0.2838	3.5856	3.6170	0.9913	169.45	0.01058	0.01509	0.00398	−0.00419	1.05186	−0.00021
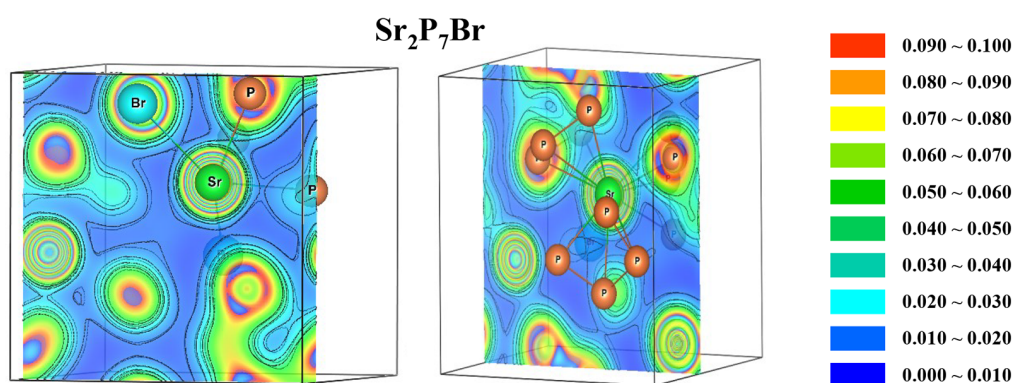
Sr_2P_7Br

Figure 5. The electronic charge density map depicting the bonding characteristics in the Sr_2P_7Br compound.

charge density, which represents the second spatial derivative of the charge density, indicates that the value of the charge density at the critical point of the bond is greater than the average value of the surrounding areas (i.e., a covalent bond). Conversely, the positive sign of the Laplacian of the charge density implies the opposite. The value of the local kinetic energy density of electrons is always positive and expresses the delocalization of the charge or electrons at the critical point. Its value indicates the extent of restriction, freedom of movement, and speed of this charge (electrons) between the two atoms; the higher its value, the greater the presence of repulsive forces. The larger the absolute value of V_b, which represents the electrostatic potential energy density between the atomic nuclei and the charge at the critical point, the more strongly the charge is bound to the surrounding nuclei and the more stable the bond. A more negative value of Hb, which represents the total density of kinetic and potential energy, indicates greater stability of the bonds.

A tool that is utilized for the purpose of analyzing the structure of molecules and gaining an understanding of their chemical topology is the attractor connectivity matrix. By utilizing the attractor connectivity matrix, it is feasible to determine which atoms are responsible for a particular relationship between

them, as well as the strength of the bonds that are produced by each individual atom. Based on the informationprovided by this matrix, it is evident that the diatomic pairings that interact the most strongly are P—P, Sr—Br, Sr—P, and Br—P.

$$\begin{pmatrix} & P & P & Sr & Sr & Br & P \\ P & 2 & 1 & 1 & 2 & 1 & 1 \\ P & 1 & 2 & 1 & 0 & 1 & 1 \\ Sr & 3 & 3 & 0 & 0 & 3 & 1 \\ Sr & 6 & 0 & 0 & 0 & 1 & 0 \\ Br & 3 & 3 & 3 & 1 & 0 & 0 \\ P & 3 & 3 & 1 & 0 & 0 & 0 \end{pmatrix}$$

3.3. Attractor Connectivity Matrix

The estimated values of the QTAIM descriptors for the examined material are presented in Table 2. The computed electron density values for all considered bonds, given in Table 2, demonstrate that the P—P bond exhibits the highest electron density at the BCP, surpassing 0.07 e.Å^{-3}, whereas the other bonds do

ChemistrySelect

Research Article
doi.org/10.1002/slct.202502428

Chemistry Europe
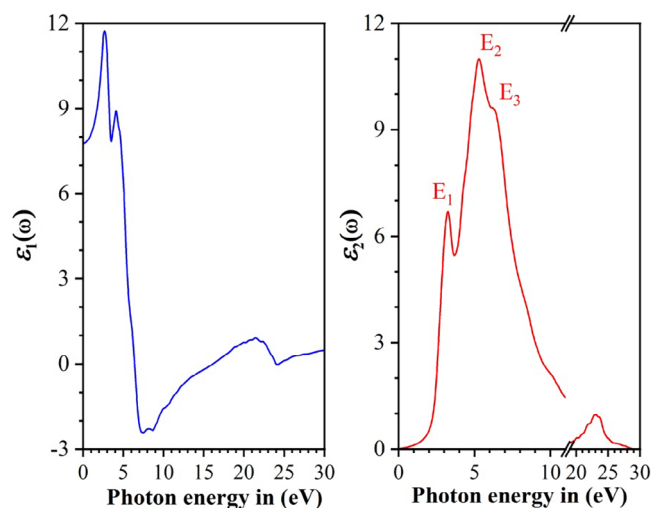European Chemical
Societies Publishing

Figure 6. The spectra of the components of the complex dielectric function ($\varepsilon(\omega) = \varepsilon_1(\omega) + i\varepsilon_2(\omega)$) for Sr_2P_7Br. The computations were executed utilizing the TB-mBJ method to model the XC potential.

not reach 0.02 e.Å^{-3}. The charge density distribution in Sr_2P_7Br, analyzed and illustrated in Figure 5, reveals minimal charge densities at the BCP of the Sr—P and Sr—Br bonds, which do not exceed 0.02 e.Å^{-3}. The ratio $R = r_1/r_2$ (where r_1 and r_2 stand to the distances between the BCP and the bond endpoints E1 and E2, respectively) in the P—P bond is equal to one, thereby affirming the critical point's central position between the two nuclei and substantiating the covalent nature of this bond. A bond is considered to have polarization when the ratio $R = r_1/r_2$ is very close to unity with little variation. The angle $\hat{\alpha} = $ E1 − BCP − E2, where the vertex at BCP and sides extending across the two atoms E1 and E2, indicates that the Sr—CBP—P and Ba—CBP—P angles for the Sr—P and Ba—P bonds measure 180 degrees. In contrast, the angles for the other bonds are different of 180°, with a maximum deviation of 14.50 ° from the straight angle of 180° for

the Ba—P bonds. According to the QTAIM descriptors at BCPs, an ionic bond is defined by a lack of local charges along the critical bond path. This bond type is distinguished by a low ρ_b at BCPs, a positive value of H_b and a negative value of V_b with an absolute value of V_b comparable to the value of G_b ($|V_b| \approx G_b$). A covalent bond is established through the aggregation of localized charges. This bond exhibits a high ρ_b at BCPs, $H_b \ll 0$, and possesses a negative V_b ($V_b \ll 0$), which has a markedly lower absolute value than the kinetic G_b ($|V_b| \ll G_b$).[10,42–45] Based on the results presented in Table 2, there is a concentration of local charge at the critical point of the P—P bond, where the electron density is significantly elevated compared to other bonds, which exhibit a depletion of local charge at their critical points. Furthermore, the ratio $|\mathbf{V_b}|/\mathbf{G_b}$ for the P—P bond largely exceeds 1, indicating that $|\mathbf{V_b}| > > \mathbf{G_b}$. Additionally, the total charge density is negative, in contrast to the other bonds Sr—Br, Sr—P, and Br—P, where the absolute value of V_b ($|V_b|$) is approximately equal to G_b. Moreover, H_b is minimal and positive. Consequently, it can be asserted that the bonds in the Sr_2P_7Br compound are of a mixed nature, with P—P bonds being covalent and Sr—Br, Sr—P, and Br—P bonds being ionic.

3.4. Optical Characteristics

Figure 6 illustrates the $\varepsilon_2(\omega)$ spectrum of the examined material throughout the energy range of 0–30 eV, which derived using the TB-mBJ functional to model the exchange-correlation potential. Identifying the electronic transition origins of the structures in the $\varepsilon_2(\omega)$ curve is of fundamental importance. The $\varepsilon_2(\omega)$ curve arises from permitted electronic transitions from occupied states to unoccupied ones. Electron transitions in semiconductors occur between filled levels in the valence band (VB) and the empty ones in the conduction band (CB). To ascertain the origins of the electronic transitions yielding the $\varepsilon_2(\omega)$ spectrum, it

Table 3. Locations of the central points of the primary structures in the $\varepsilon_2(\omega)$ spectrum, together with the predominant interband electronic transitions (V_i-C_j) contributing to each structure for Sr_2P_7Br. The enumeration of the bands is up (down) from the CBM (VBM) point. Predominant contributions from interband transitions.

Optical structures		Predominant interband transitions	
Structure	Center (eV)	Vi – Cj	Contribution center (eV)
E_1	3.24	V_1-C_2/ V_1-C_3/V_1-C_3	2.54/2.69/2.80
		V_1-C_6/V_1-C_7/V_1-C_8	2.99/3.14/2.69
		V_2-C_2/V_2-C_4/V_2-C_{10}	2.83/3.30/2.83
		V_3-C_4/V_3-C_7/V_3-C_{10}	3.14/3.30/3.14
		V_5-C_3	
E_2	5.28	V_1-C_{31}/V_1-C_{33}/V_1-C_{34}	4.83/4.86/4.79
		V_2-C_{36}/V_2-C_{37}	5.12/5.12
		V_6-C_{25}/V_6-C_{26}/V_6-C_{27}	4.83/4.67/4.86
		V_7-C_{17}/V_7-C_{19}	4.21/4.37
		V_8-C_{17}	4.21
E_3	6.25	V_1-C_{57}/V_1-C_{59}	6.19/6.19
		V_2-C_{54}/V_2-C_{55}/V_2-C_{58}/V_2-C_{59}	6.35/6.22/6.38/6.50
		V_3-C_{58}/V_4-C_{57}/V_4-C_{58}/V_4-C_{59}	6.50/6.50/6.35/6.35
		V_5-C_{50}/V_5-C_{52}/V_5-C_{54}/V_5-C_{55}/V_5-C_{56}	6.19/6.35/6.29/6.53/6.35
		V_6-C_{53}/V_6-C_{54}/V_6-C_{60}	6.50/6.50/6.84
		V_7-C_{49}/V_7-C_{50}/V_7-C_{51}/V_7-C_{52}/V_7-C_{53}	6.19/6.38/6.35/6.35/6.50
		V_7-C_{56}/V_7-C_{57}/V_7-C_{58}/V_7-C_{59}/V_7-C_{60}	6.50/6.66/6.63/6.81/6.80

ChemistrySelect

Research Article
doi.org/10.1002/slct.202502428

Chemistry Europe
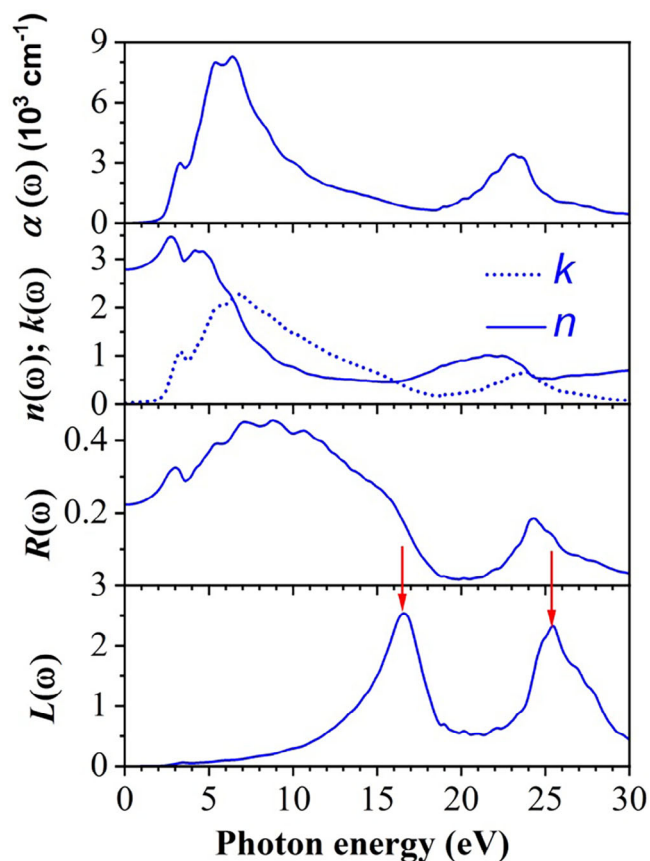European Chemical
Societies Publishing

Figure 7. The computed spectra of the linear optical functions, specifically the absorption coefficient $\alpha(\omega)$, refractive index $n(\omega)$, extinction coefficient $k(\omega)$, optical reflectivity $R(\omega)$, and electron energy loss $L(\omega)$, for the Sr_2P_7Br compound, derived using the TB-mBJ potential to model the XC potential.

is essential first to identify the pairs of bands involved in these transitions, i.e., the transitions $V_i \rightarrow C_j$, where V_i is a valence band C_j is a conduction band. The band pairs (V_i–C_j) that predominantly contribute to the main structures in the $\varepsilon_2(\omega)$ spectrum are listed in Table 3.

The $\varepsilon_1(\omega)$ curve for the material being investigated is also illustrated in Figure 6. The static dielectric constant $\varepsilon(0) = \varepsilon_1(\omega \rightarrow 0)$[47,48] is measured to be 7.78.

Figure 7 displays the calculated curves of the linear optical coefficients for the compound Sr_2P_7Br, specifically the complex refractive index ($n(\omega)$, and $k(\omega)$), absorption coefficient ($\alpha(\omega)$), optical reflectivity ($R(\omega)$), and electron energy loss ($L(\omega)$).

From the $\alpha(\omega)$ curve, one notes that Sr_2P_7Br has significant photon absorption within the energy spectrum from about 3–10 eV. This optical behavior renders Sr_2P_7Br highly effective as a filter for radiation within the 3–10 eV energy range. Note that Sr_2P_7Br exhibits maximal absorption of electromagnetic radiation at an energy of around 6.5 eV.

The refractive index, represented by the symbol $n(\omega)$, is an essential optical characteristic that serves to define the manner in which electromagnetic radiation travels through a medium.[49] More specifically, it quantifies the decrease in the light phase velocity that occurs within the medium. When considering the compound Sr_2P_7Br, it is seen that $n(\omega)$ exhibits a significant

dependence on the incident photon energy. The $n(\omega)$ curve shows a gradual increase from its static value of 2.8 as photon energy increases. Note that when the photon energy approaches the absorption edge, there is a significant rise in the value of $n(\omega)$, peaking at 3.47 when the photon energy reaches 2.69 eV, after which the refractive index decreases with further increases in photon energy.

This behavior is crucial for uses that exploit Sr_2P_7Br's optical properties. The variation in refractive index with photon energy affects the material's interaction with light across a range of wavelengths. It is essential to recognize that Sr_2p_7br possesses numerous energy levels at which the extinction coefficient, denoted by $k(\omega)$, reaches its maximum value. Sr_{2P7Br} attains a maximum $k(\omega)$ value of 2.31 at an energy level of 6.77 eV.

The material in question exhibits a reflectance greater than 20% across an energy range of 0 to 16. The electron energy loss $L(\omega)$ is essential when describing the energy dissipation that occurs when high-velocity electrons pass through a material.[50] The $L(\omega)$ spectrum displays two plasma peaks at 16.5 and 25.4 eV, which correspond to the sharp decline in the reflectivity curve.

3.5. Thermoelectric Characteristics

How charge carriers react to heat is essential for evaluating how a material can be used in electrical or thermal conductivity, especially if the material is semi-conductive. Due to the classification of Sr_2P_7Br as a semiconductor compound, our focus was directed toward the investigation of its thermoelectric qualities. The key thermoelectric parameters, which are essential for evaluating the suitability of a material for use in thermoelectric applications, are the Seebeck coefficient (S), thermal and electrical conductivities (k, and σ), power factor ($PF = S^2\sigma$), and figure of merit ($ZT = \sigma S^2 T/k$). The semi-classical Boltzmann transport model within the rigid band approach (RBA) and constant scattering time approximation (CRTA),[34,35,51] as integrated in the BoltzTraP2 program,[33] was utilized to accomplish this purpose. The results obtained regarding the variations of the above-mentioned parameters versus the charge-carrier concentration at constant temperature are illustrated in Figure 8.

The curve representing S versus charge-carrier concentration indicates that the S value for electrons surpasses that of holes at identical temperature and concentration. The S value surpasses 0.5 mV K^{-1} for electron concentration of 10^{21} cm^{-3} at a temperature of 300 K. For both types of charge carriers, S shows a decreasing trend with increasing concentration.

In reference to the roles of electrons and holes in electrical and thermal conductivity, Figure 8 illustrates that both increase as the concentration of charge-carriers rises. Nevertheless, it was observed that, at the same concentration, thermal conductivity exhibits an increase with rising temperature, whereas electrical conductivity demonstrates a decline as temperature escalates. Figure 8 indicates that holes show superior thermal and electrical conductivity in comparison to electrons when assessed at identical temperature and concentration levels. The small mass of holes explains that, compared to electrons, holes have greater mobility than electrons ($m_h^*((R - M) \rightarrow R) = 0.5253$ and
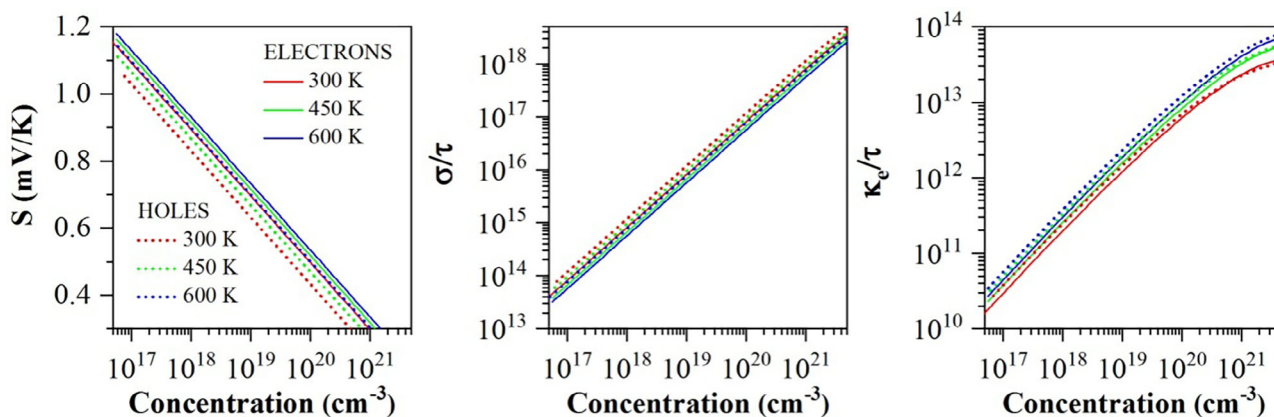
ChemistrySelect

Research Article
doi.org/10.1002/slct.202502428

Chemistry Europe
European Chemical
Societies Publishing

Figure 8. Variations of the Seebeck coefficient (S, in mV K^{-1}), electronic thermal conductivity (k_e, in W^{-1} m^{-1} K^{-1}), and electrical conductivity (σ, in Ω^{-1} cm^{-1}) versus charge-carrier concentration at specified temperatures T: 300, 450, and 600 K for Sr$_2$P$_7$Br. τ (measured in s) is the relaxation time.
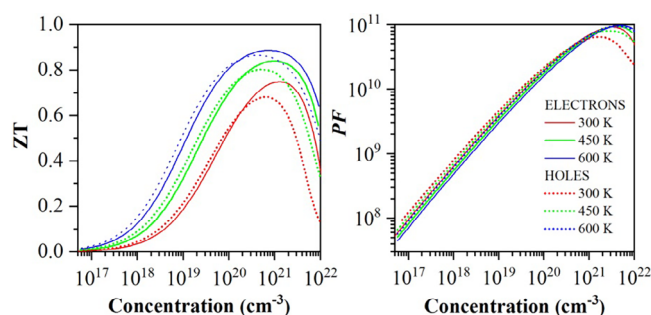
Figure 9. Variations of the power factor (PF, measured in W cm^{-1} s^{-1} K^{-2}) and figure of merit (ZT) versus charge-carrier concentration at selected temperatures T: 300, 450, and 600 K for Sr$_2$P$_7$Br.

$m_h^*((R-M) \to M) = 0.2776$, $m_e^*(R \to M) = 1.1024$ and $m_e^*(R \to X) = 1.7343$).

Figure 9 illustrates the variations of PF and ZT versus charge-carrier concentrations at constant temperatures of 300, 450, and 600 K. The holes and electrons achieve a ZT exceeding 0.6 at a concentration of 10^{21} cm^{-3} at a temperature of 300 K. At the same concentration, this value increases to 0.9 at a temperature of 600 K. This renders the examined chemical auspicious for application in the thermoelectric domain. Figure 9 indicates that n-doping Sr$_2$P$_7$Br exhibits a superior figure of merit compared to p-doping Sr$_2$P$_7$Br.

4. Conclusion

The structural, electronic, optical, and thermoelectric qualities of Sr$_2$P$_7$Br, a Zintl material, were predicted employing the FP-LAPW approach. The analysis of the computed energy band structure indicates that Sr$_2$P$_7$Br is a semiconductor with an indirect band gap of 1.947 eV when employing the GGA-PBEsol functional for modeling exchange-correlation interactions, and 2.432 eV when utilizing the TB-mBJ potential, which was specifically designed to address the bandgap underestimate inherent in the GGA. The examination of the PDOS curves and charge density map reveals that the interaction between Sr cations and P and Br anions is primarily ionic. Conversely, the P—P linkage within

the [P_7^{3-}] unit and the P–Br bond are predominantly covalent. Based on the expected macroscopic optical properties, Sr$_2$P$_7$Br could have applications in optical devices because it can absorb UV light while remaining transparent in the visible spectrum. Furthermore, the thermoelectric analysis reveals that n-doped Sr$_2$P$_7$Br is preferable to p-doped Sr$_2$P$_7$Br for better thermoelectric efficiency. The material's figure of merit reaches 0.9 for an electron concentration of 10^{21} cm^{-3} at 600 K. Our findings represent theoretical predictions that require validation through future experimental studies.

Conflict of Interests

The authors declare no conflict of interest.

Data Availability Statement

All data in the manuscript.

[1] S. R. Watts, L. M. Wingate, S. Bobev, S. Baranets, *Crystals* **2024**, *14*, 570.

[2] A. Khireddine, A. Bouhemadou, S. Alnujaim, N. Guechi, S. Bin-Omran, Y. Al-Douri, R. Khenata, S. Maabed, A. K. Kushwaha, *Solid State Sci.* **2021**, *114*, 106563.

[3] N. Guechi, A. Bouhemadou, Y. Medkour, Y. Al-Douri, R. Khenata, S. Bin-Omran, *Philos. Mag.* **2020**, *100*, 3023–39.

[4] A. Khireddine, A. Bouhemadou, S. Maabed, S. Bin-Omran, R. Khenata, Y. Al-Douri, *Solid State Sci.* **2022**, *128*, 106893.

[5] K. Ghosh, S. Rahman, A. Ovchinnikov, S. Bobev, *Inorg Chem.* **2024**, *63*, 20173–20185.

[6] A. I. Aljameel, G. M. Mustafa, B. Younas, H. D. Alkhaldi, F. Alhajri, G. I. Ameereh, N. Sfina, A. S. Alshomrany, Q. Mahmood, *J. Phys. Chem. Solids* **2024**, *189*, 111953.

[7] Z. Zhang, J. Li, H. Yao, Q. Wang, L. Yin, K. Liu, X. Ma, M. Yuan, R. Wang, S. Duan, *Acta Mater.* **2024**, *268*, 119777.

[8] Q. Xu, K. Zhao, H. Huang, S. Wan, Q. Ren, X. Hao, H. Wuliji, J. Lei, T.-R. Wei, X. Shi, *Acta Mater.* **2024**, *274*, 120040.

[9] S. Al-Essa, S. S. Essaoud, A. Bouhemadou, M. E. Ketfi, S. Bin-Omran, A. Chik, M. Radjai, D. Allali, R. Khenata, Y. Al-Douri, *J. Inorg. Organomet. Polym. Mater.* **2024**, *34*, 4174–4191.

[10] S. El-Essa, S. E. Saber, A. Bouhemadou, M. E. Ketfi, S. Maabed, F. Djilani, S. Bin-Omran, M. Radjai, D. Allali, R. Khenata, Y. Al-Douri, *Phys. Scr.* **2024**, *99*, 095996.

[11] C. K. Vishwakarma, M. Zeeshan, B. K. Mani, *J. Phys. Chem. C* **2024**, *128*, 2311–2320.

[12] J. Mangeri, M. Ovesen, T. Olsen, *Phys. Rev. B* **2024**, *109*, 214404.

[13] M. Ishtiyak, S. G. K. Samarakoon, T. K. Don, S. R. Watts, S. Baranets, *Nanoscale* **2024**, *16*, 7916–25.

[14] C. Chen, X. Li, W. Xue, F. Bai, Y. Huang, H. Yao, S. Li, Z. Zhang, X. Wang, J. Sui, *Nano Energy* **2020**, *73*, 104771.

[15] L. Borgsmiller, Q. Li, M. Y. Toriyama, G. Snyder *J. Adv. Energy Mater.* **2023**, *13*, 2300393.

[16] T. Zhou, Z. Feng, J. Mao, J. Jiang, H. Zhu, D. J. Singh, C. Wang, Z. Ren, *Chem. Mater.* **2020**, *32*, 776–84.

[17] K.-F. Liu, S.-Q. Xia, *J. Solid State Chem.* **2019**, *270*, 252–264.

[18] Z. M. Elqahtani, S. Aman, S. Mehmood, Z. Ali, A. Hussanan, N. Ahmad, S. Alomairy, M. S. Al-Buriahi, Z. A. Alrowaili, H. M. T. Farid, *J. Taibah Univ. Sci.* **2022**, *16*, 660–9.

[19] J. Cheng, C. Duan, Y. Du, J. Duan, M. Qi, Y. Chen, L. Yang, W. Duan, S. Zhang, P. Lin, *J. Mater. Sci.* **2025**, *8*, 1–14.

[20] S. D. Günay, Ü. Akdere, Ç. Taşseven, *Mater. Today Commun* **2025**, *45*, 112276.

[21] M. P. Hautzinger, S. Quadir, B. Feingold, R. Seban, A. J. Thornton, N. S. Dutta, A. G. Norman, L. I A, M. R. Hasan, K. A. Kovnir, *ACS Nano* **2025**, *19*, 12345–53.

[22] H. D. Alkhaldi, G. M. Mustafa, B. Younas, S. Bouzgarrou, A. I. Aljameel, M. M. Al-Anazy, Q. Mahmood, I. Boukhris, M. S. Al-Buriahi, *J. Phys. Chem. Solids* **2025**, *203*, 112737.

[23] T. M. Al-Daraghmeh, G. M. Mustafa, B. Younas, O. Zayed, S. Bouzgarrou, I. Boukhris, M. M. Al-Anazy, M. S. Al-Buriahi, Q. Mahmood, *Opt. Quantum Electron.* **2025**, *57*, 1–18.

[24] J.-A. Dolyniuk, K. Kovnir, *Crystals* **2013**, *3*, 431–42.

[25] J. Dolyniuk, N. Tran, K. Lee, K. Kovnir, *Z. Für Anorg. Allg. Chem.* **2015**, *641*, 1422–7.

[26] P. Blaha, K. Schwarz, F. Tran, R. Laskowski, G. K. Madsen, L. D. Marks, *J. Chem. Phys.* **2020**, *152*, 074101.

[27] J. P. Perdew, A. Ruzsinszky, G. I. Csonka, O. A. Vydrov, G. E. Scuseria, L. A. Constantin, X. Zhou, K. Burke, *Phys. Rev. Lett.* **2008**, *100*, 136406.

[28] F. Tran, P. Blaha, *Phys. Rev. Lett.* **2009**, *102*, 226401.

[29] D. Koller, F. Tran, P. Blaha, *Phys. Rev. B* **2011**, *83*, 195134.

[30] C. A. Mead, *Phys. Rev.* **1962**, *128*, 2088–93.

[31] C. Ambrosch-Draxl, J. O. Sofo, *Comput. Phys. Commun.* **2006**, *175*, 1–14.

[32] S. Z. Karazhanov, P. Ravindran, A. Kjekshus, H. Fjellvåg, B. G. Svensson, *Phys. Rev. B* **2007**, *75*, 155104.

[33] G. K. Madsen, J. Carrete, M. J. Verstraete, *Comput. Phys. Commun.* **2018**, *231*, 140–145.

[34] T. Fang, S. Zheng, T. Zhou, H. Chen, P. Zhang, *J. Electron. Mater.* **2017**, *46*, 3030–3035.

[35] M.-S. Lee, S. D. Mahanti, *Phys. Rev. B* **2012**, *85*, 165149.

[36] F. Birch, *J. Geophys. Res. Solid Earth* **1978**, *83*, 1257–1268.

[37] M. Radjai, S. Saad Essaoud, A. Bouhemadou, D. Allali, A. Bedjaoui, *Comput. Theor. Chem.* **2024**, *1242*, 114947.

[38] F. Firdous, S. M. Qaid, A. S. Aldwayyan, A. A. A. Ahmed, J. Munir, *J. Magn. Magn. Mater.* **2024**, *611*, 172611.

[39] C. F. Matta, R. J. Boyd, *Quantum Theory At. Mol. Solid State DNA Drug Des*, Wiley-VCH Verlag GmbH & Co. KGaA, Weinheim, Germany **2007**.

[40] R. F. W. Bader, T. T. Nguyen-Dang, Y. Tal, *Rep. Prog. Phys.* **1981**, *44*, 893.

[41] A. Otero-de-la-Roza, E. R. Johnson, V. Luaña, *Comput. Phys. Commun* **2014**, *185*, 1007–18.

[42] S. S. Essaoud, S. M. Al Azar, A. A. Mousa, R. S. Masharfe, *Phys. Scr.* **2023**, *98*, 035820.

[43] R. Bianchi, G. Gervasio, D. Marabello, *Inorg. Chem.* **2000**, *39*, 2360–6.

[44] S. Chanda, R. Maity, S. Saha, A. Dutta, T. P. Sinha, *J. Sol-Gel Sci. Technol.* **2021**, *99*, 600–613.

[45] S. Sâad Essaoud, S. M. Al Azar, A. A. Mousa, A. Y. Al-Reyahi *Phys. Scr.* **2023**, *98*, 035820

[46] H. Tributsch, *Z. Für Naturforschung A* **1977**, *32*, 972–985.

[47] K. M. Wong, W. Khan, M. Shoaib, U. Shah, S. H. Khan, G. Murtaza, *J. Electron. Mater.* **2018**, *47* 566–76.

[48] A. Bouhemadou, S. Al-Essa, D. Allali, M. A. Ghebouli, S. Bin-Omran, *Solid State Sci.* **2013**, *20*, 127–34.

[49] D. R. Penn, *Phys. Rev* **1962**, *128*, 2093.

[50] D. Allali, A. Bouhemadou, E. M. A. Al Saf, S. Bin-Omran, M. Chegaar, R. Khenata, A. H. Reshak, *Phys. B Condens. Matter* **2014**, *443*, 24–34.

[51] K. Boudiaf, A. Bouhemadou, Y. Al-Douri, R. Khenata, S. Bin-Omran, N. Guechi, *J. Alloys Compd.* **2018**, *759*, 32–43.